Supplementary Information

On the origin of initial hydrocarbons in methanol-to-hydrocarbons reaction

Teng Li[1], Sang-Ho Chung[1], Stefan A. Nastase[1], Xiangkun Wu[2], Zihao Zhang[2], Rushana Khairova[1], Andras Bodi[2], Patrick Hemberger[2]*, Jorge Gascon[1], Luigi Cavallo[1], and Javier Ruiz-Martínez[1]*

[1]KAUST Catalysis Center, King Abdullah University of Science and Technology, Thuwal 23955, Saudi Arabia.

[2]Paul Scherrer Institute, CH-5232 Villigen, Switzerland

*e–mail: javier.ruizmartinez@kaust.edu.sa; patrick.hemberger@psi.ch

Table of Contents

SI │ Materials and Methods

Zeolites preparation

The commercial ZSM-5 zeolite (NH_4-form) with a Si/Al ratio of 11.5 was purchased from ZEOLYST (CBV 2314). The zeolite was calcined in air at 550 °C for 10 h with a heat ramp of 2 °C min^{-1}, to obtain its protonic form, HZSM-5. Home-made FeHZSM-5 was prepared by one-pot synthesis method in which the Fe-containing precursor was added at the beginning of zeolite synthesis.

Temperature programmed surface reaction (TPSR) of pre-adsorbed molecules

Temperature-programmed surface reaction (TPSR) of methanol was performed in a cell connected to a mass spectrometer (INFICON, ionization energy 70 eV). Helium (> 99.999%) was utilized as the carrier gas, since helium (*m*/*z* 4) has no overlap with the main products or intermediates in the methanol conversion. Around 40 mg of zeolite sample were pretreated at 500 °C for 1 h in a helium flow (20 mL/min) with a heating rate of 10 °C /min. The sample was then cooled to 50 °C, stabilized for 10 mins, and then loaded with methanol for 30 min using helium as carrier gas. After that, the sample was purged with pure helium for 30 min to eliminate the physiosorbed methanol. Methanol–TPSR experiments were performed in the temperature range of 50–500 °C with a heating rate of 5 °C /min. The gas phase products were analyzed by mass spectrometry (MS), referred to the database of the National Institute of Standards and Technology (NIST). The *m*/*z* values of the reactant and products were as follows: methanol (31), hydrogen (2, after deducting the fragment signal of methanol), methane (16, after deducting the fragment signal of methanol), ethylene (27), formaldehyde (30, after deducting the fragment signal of methanol), propylene (41), CO_2 or acetaldehyde (44), dimethyl ether (45), acetic acid (60, not observed), methyl acetate (74, not observed), benzene (78, not observed), and toluene (91, not observed). During the methanol–TPSR experiment, *operando* diffuse reflectance infrared Fourier transform spectroscopy (DRIFTS) spectra were recorded as well, using a Nicolet 6700 FT-IR Spectrometer with a liquid-N_2 cooled MCT detector. To exclude the influence caused by temperature variation, spectra of bare zeolite after pretreatment were collected first in a helium flow at different corresponding temperatures and used as background.

For the $^{13}CH_3OH$–TPSR experiment, similar operations were conducted. The *m*/*z* values of the reactant and products were as follows: methanol (32), hydrogen (2, after deducting the fragment signal of methanol), formaldehyde (31, after deducting the fragment signal of methanol), propylene (45, 44, 43, 42), CO_2 (45), acetaldehyde (46, 45), and dimethyl ether (47).

For the formic acid–TPSR experiment, the *m*/*z* values of the reactant and products were as follows: formic acid (46, 45, 44, 2), hydrogen (2), ethylene (27, not observed), and propylene (41, not observed), and CO_2 (44).

For the acetaldehyde–TPSR experiment, the *m*/*z* values of the reactant and products were as follows: acetaldehyde (44), hydrogen (2, after deducting the fragment signal of acetaldehyde), ethylene (27, after deducting the fragment signal of acetaldehyde), methanol (31, not observed), propylene (41, after deducting the fragment signal of acetaldehyde), CO_2 (44) and dimethyl ether (45, not observed).

For the acetic acid–TPSR experiment, the *m*/*z* values of the reactant and products were as follows: acetic acid (60), hydrogen (2, after deducting the fragment signal of acetic acid), ethylene (27, after deducting the fragment signal of acetic acid), methanol (31, not observed), propylene (41, after deducting the fragment signal of acetic acid), and CO_2 (44, after deducting the fragment signal of acetic acid).

For the methyl acetate–TPSR experiment, the *m*/*z* values of the reactant and products were as follows: methyl acetate (74), hydrogen (2, after deducting the fragment signal of methyl acetate), ethylene (27, after deducting the fragment signal of methyl acetate), methanol (31), propylene (41, after deducting the fragment signal of methyl acetate), and dimethyl ether (45).

Operando photoelectron photoion coincidence spectroscopy (PEPICO)

Operando photoelectron photoion coincidence spectroscopy (PEPICO) experiments were carried out using the CRF-PEPICO endstation at the vacuum ultraviolet beamline of the Swiss Light Source of the Paul Scherrer Institute, Switzerland. The catalyst was loaded into a tubular quartz reactor (2 mm internal diameter). At the reactor outlet, reaction intermediates and products form a molecular beam. After the beam passes through a skimmer, monochromatic vacuum ultraviolet (VUV) radiation ionizes the molecules. The resulting photoelectrons and photoions are accelerated in opposite directions by a constant electric field and are detected in delayed coincidence. Thanks to the negligible electron time of flight (TOF), TOF mass spectrometry can be used to determine the mass-to-charge (*m*/*z*) ratio of photoions. Photoelectrons are also kinetic energy analyzed using velocity map imaging. Photoion mass-selected threshold photoelectron (ms-TPE) spectra can, thus, be derived by only accepting electrons with a low kinetic energy ($< (5–10) \times 10^{-3}$ eV).

For the TPSR experiments conducted under continuous flow conditions, the catalyst was first pretreated in argon flow at 500 °C for 1 hour prior to PEPICO experiments, and an empty quartz reactor was used for reference. The sample was then cooled to 150 °C overnight, stabilized for 10 mins, and then fed with methanol using argon as carrier gas. The total gas flow rate (F_T) was adjusted to 22 cm^3 STP min^{-1} with CH_3OH:Ar = 1:21. The methanol–TPSR experiment was performed in the range of 150–500 °C with a heating rate of 5 °C/min. The temperature was increased in 20 °C steps. Since the quartz reactor was placed in a vacuum chamber (10^{-4} mbar), thermal conduction was drastically reduced. Therefore, the activated catalyst after thermal treatment at 500 °C did not cool to 50 °C overnight. This constrained the starting

temperature of TPSR to 150 °C. Nevertheless, we expect that this starting temperature would not affect the whole chemistry since the first olefins are not formed at 150 °C.

The isothermal reaction tests were performed in the range of 200–300 °C. After cooling to the specific reaction temperature after pretreatment, the catalyst was fed with methanol. Meanwhile, the ms-TPE spectra started to be collected, and the photon energy was scanned in the 8.8-10.7 eV range with a step of 0.03 eV. When comparing ms-TPE spectra with Franck-Condon simulations or reference spectra, the ionization energies and the vibrational fingerprints in the spectra identify the molecular structure of the spectral carrier and enable isomer-selective detection.

Solid-state nuclear magnetic resonance (ssNMR) spectroscopy

The samples for NMR measurements were prepared using the cell for TPSR experiments. The zeolite was pretreated at 500 °C for 1 h in a helium flow and then cooled to a specific temperature, stabilized for 10 mins, and then loaded with ^{13}C labeled methanol for 30 min using helium as carrier gas. After that, the reaction was stopped, and the sample was cooled down either with a helium flow for 5 min or without any gas purging. The sample was immediately loaded in the rotor.

All solid-state NMR experiments related to ^{1}H and ^{13}C were conducted on an AVANCE-III console equipped with a 3.2 mm HXY probe in the double channel ^{1}H, ^{13}C mode on a Bruker 600 MHz wide-bore magnet. All experiments were conducted at room temperature (298 K) and at a MAS frequency of 20 kHz. ^{1}H and ^{13}C chemical shifts were referenced externally to adamantane. The 1D ^{1}H-^{13}C cross-polarization (CP) spectrum was recorded with a 4 s recycle delay and a 33 ms acquisition time. During the CP step, ^{1}H CP spin-lock pulses centered at 75 kHz were linearly ramped from 70 to 100% and the ^{13}C RF field was matched to obtain an optimal signal. The 1D direct excitation (DE) spectrum was acquired with a 5 s recycle delay and a 10 ms acquisition time. 2D ^{13}C-$1^{3}C$ spectra were acquired with a 2 s recycle delay, 10 ms (F2) acquisition time and an accumulation of 256 scans. ^{13}C-^{13}C mixing was achieved through proton driven spin-diffusion using phase-alternated-recoupling-irradiation-schemes (PARIS) for 120 ms. 70 kHz SPINAL64 ^{1}H decoupling was applied during both direct and indirect dimensions. 2D ^{1}H-^{13}C frequency switched Lee-Goldburg (FSLG) heteronuclear correlation spectroscopy (HETCOR) spectra were recorded with a 3 s recycle delay, 15 ms (F2) or 1.6 ms (F1) acquisition time and an accumulation of 64 scans. All NMR spectra were processed with Bruker Topspin 3.5 and analyzed using POKY software[1].

Density Functional Theory calculations

Geometry optimizations: Periodic DFT calculations were conducted using the Vienna ab initio Simulation Package (VASP)[2, 3], the Perdew−Burke−Ernzerhof functional[4] with Grimme's dispersion correction[5] (PBE-D3), and a plane-wave basis set of the projector-augmented-wave (PAW) method[6]. An energy cut-off of

600 eV was used for the expansion of the wave function in the plane wave basis set. A (1 × 1 × 1) γ-centered k-point mesh was employed to sample the first Brillouin zone and Gaussian smearing with a width of 0.5 eV. All atoms were relaxed until electronic energies varied by $< 1 \times 10^{-5}$ eV, and the forces on all atoms were < 0.01 eV $Å^{-1}$. A single unit cell of 96 T atoms was used to model the H-ZSM-5 zeolite, with a Brønsted acid site being created by substituting the T12[7, 8] site with Al and adding a charge-compensating proton. This method has been successfully employed previously to simulate zeolite adsorbate models[9, 10], with comparable results to QM/MM cluster simulations[11, 12].

Vibrational frequencies were determined by a fixed displacement method (three displacements), with the atoms of the region including the 5th nearest neighbors around Aluminum and the reactants relaxed. A scaling factor of 0.9516 referenced to the symmetric CH_3 vibrational frequency (of Brønsted acid site methoxy model) was used to adjust the calculated vibrational frequencies. Previous work implemented various scaling factors in the range of 0.9 – 0.9614[13, 14, 15, 16].

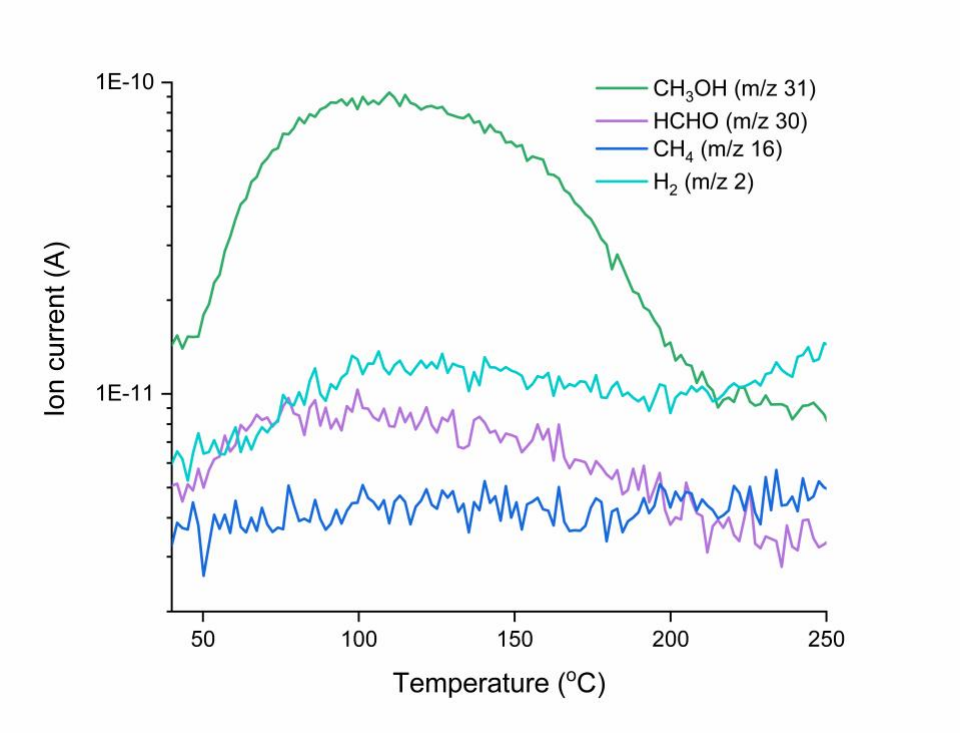

Fig. S1. Desorbed products in gas phase for the methanol–TPSR process below 250 °C to explore the origin of formaldehyde. Both formaldehyde and hydrogen were detected, while methane was not observed, indicative of methanol dehydrogenation leading to formaldehyde. Note the logarithmic y-axis.

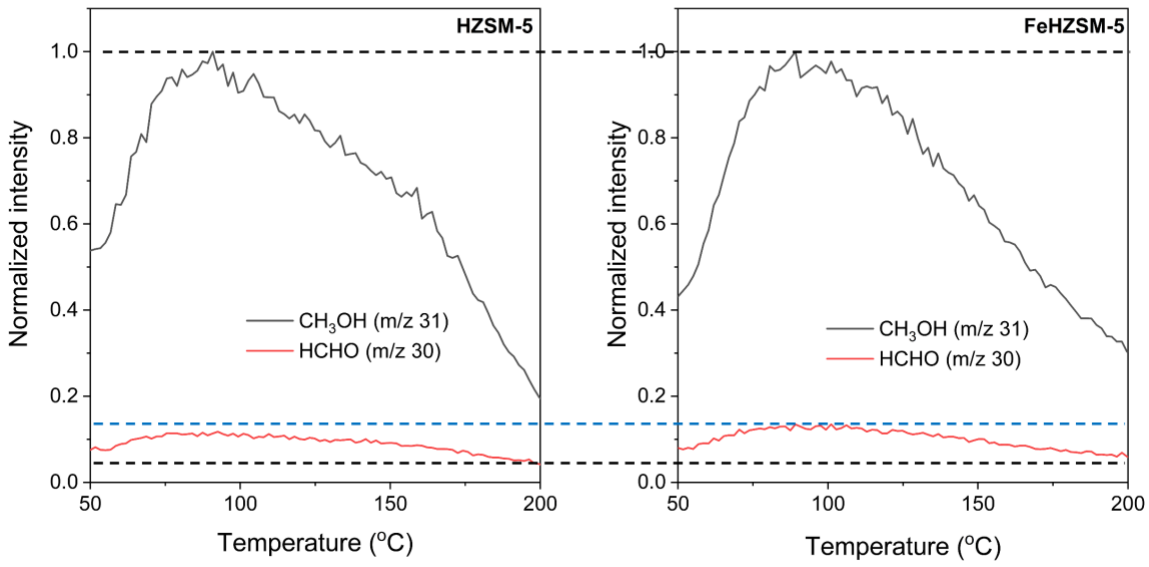

Fig. S2. Comparison of formaldehyde formation at low temperatures (< 200 °C) for the methanol–TPSR process between HZSM-5 and FeHZSM-5. The commercial HZSM-5 sample has a Fe content of around 0.02 wt.%. The FeHZSM-5 sample was prepared by one-pot synthesis method in which the Fe-containing precursor was added at the beginning of zeolite synthesis. A part of Fe atoms were expected to be incorporated into zeolite framework during crystallization. However, the subsequent zeolite calcination may help the migration of Fe atoms outside zeolite framework[17], forming small cations, clusters, or nanoparticles. The resulting FeHZSM-5 has a Fe content of 2 wt.%. Compared to HZSM-5, an increase in the formaldehyde concentration was observed over FeHZSM-5 upon heating (both after methanol fragment subtraction), although it appears that this increase is not proportional to the Fe content. A possible reason is that only a portion of Fe species with specific configurations in FeHZSM-5 can catalyze methanol dehydrogenation at such low temperatures. Exploring the structure of these active Fe species is beyond the scope of this study but is under discussion. In another methanol–TPSR experiment performed by Li et al., they also observed formaldehyde and hydrogen at low temperatures but did not provide explanations for their origin[18]. Paunovic et al. recently discovered that some transition metals in the silicon carbide diluents could lead to HCHO via methanol dehydrogenation[19]. However, this possibility can be excluded in our case, as the zeolite catalyst for TPSR study was used without any diluent. Since commercial zeolites typically contain some transition metal impurities, such as Fe[20, 21], here we examined a home-made HZSM-5 catalyst synthesized in an environment containing Fe precursor and found that Fe could promote methanol dehydrogenation. Note that the effect of other metals potentially present in the commercial catalyst cannot be excluded. Regardless, considering the facile formation of HCHO under relevant MTH conditions, irrespective originating from methanol dehydrogenation[19] or disproportionation[22], typically prior to any olefinic compounds, we speculate HCHO to be an important intermediate for the first C-C bond formation.

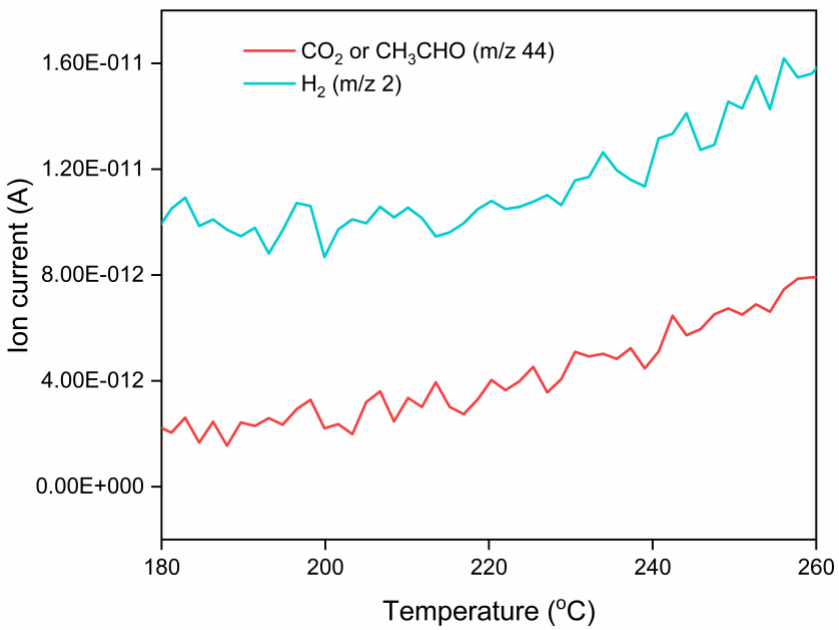

Fig. S3. Desorbed products between 180 and 260 °C for the methanol–TPSR process. With the temperature increase, the *m*/*z* 44 and *m*/*z* 2 signals show similar evolution trends.

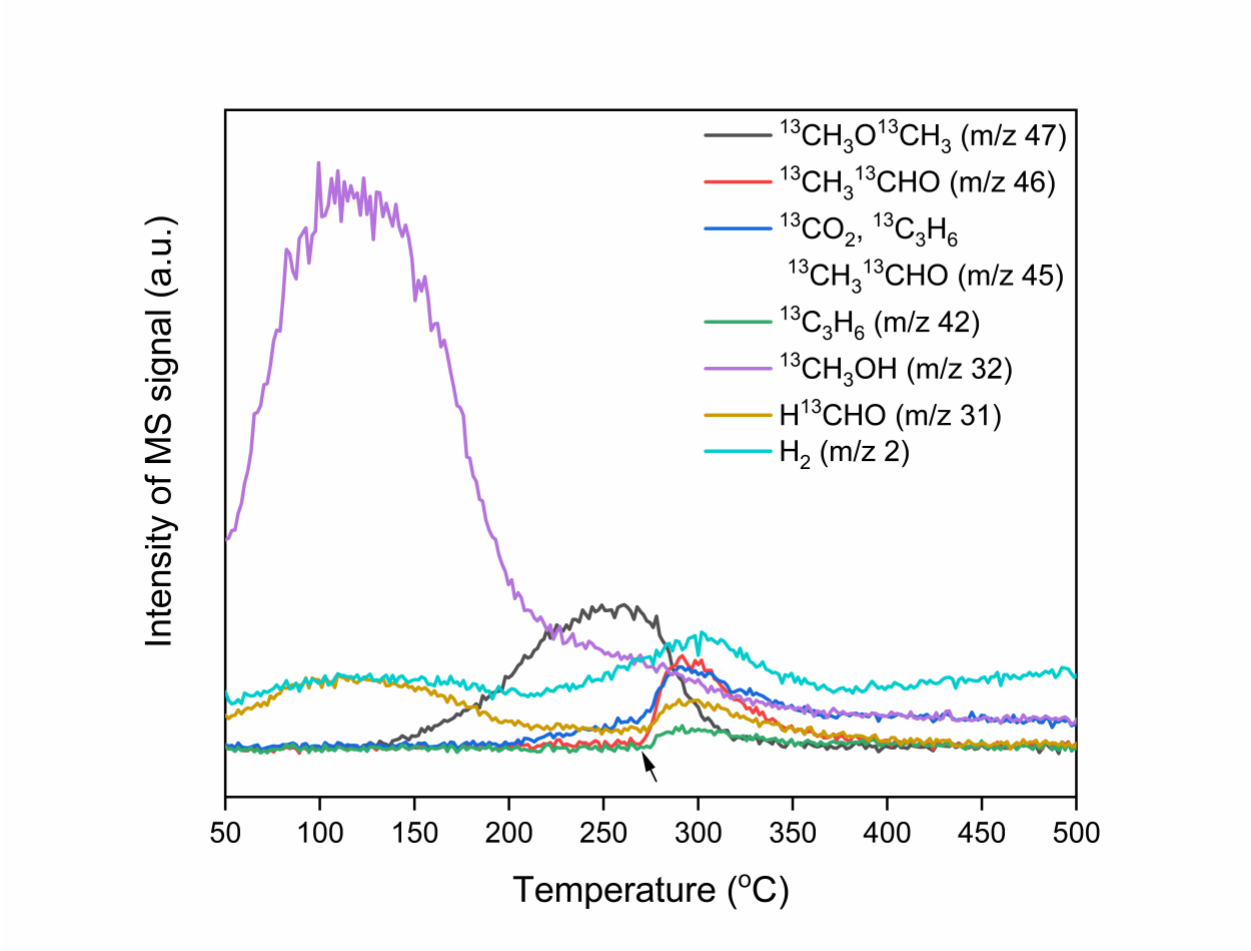

Fig. S4. Desorbed products in gas phase for the $^{13}CH_3OH$–TPSR process. The overlapping fragment signals of different species (for example, *m*/*z* 45 signal) does not allow us to distinguish species confidently. However, with the aid of observations from the previous CH_3OH–TPSR process, we could identify species of interest, as shown in **Fig. 1b** in the main text.

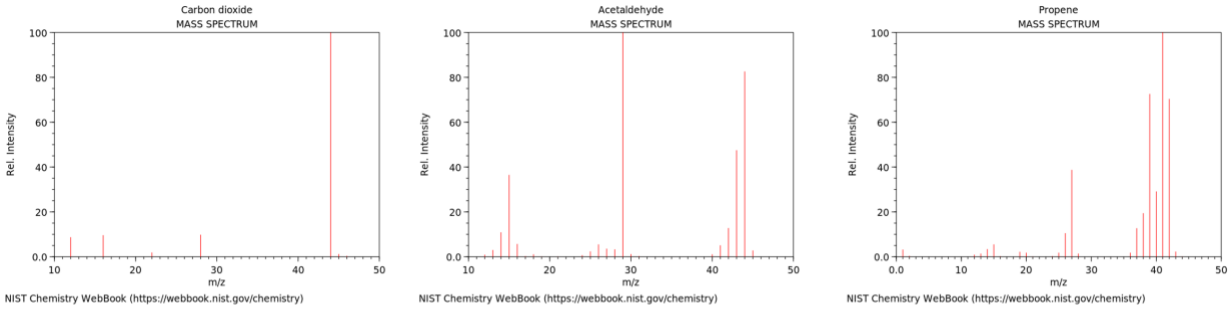

$^{12}CO_2$ signals: m/z 44

$^{13}CO_2$ signals: m/z 45

$^{12}CH_3{}^{12}CHO$ signals: m/z 44, 43

$^{13}CH_3{}^{13}CHO$ signals: m/z 46, 45

$^{12}C_3H_6$ signals: m/z 42, 41, 40, 39

$^{13}C_3H_6$ signals: m/z 45, 44, 43, 42

Fig. S5. MS spectra comparison between carbon dioxide, acetaldehyde, and propene. The standard spectra are taken from the National Institute of Standards and Technology (NIST) Mass Spectrometry Data Center. The *m*/*z* signals used in this work to distinguish species are shown below spectra.

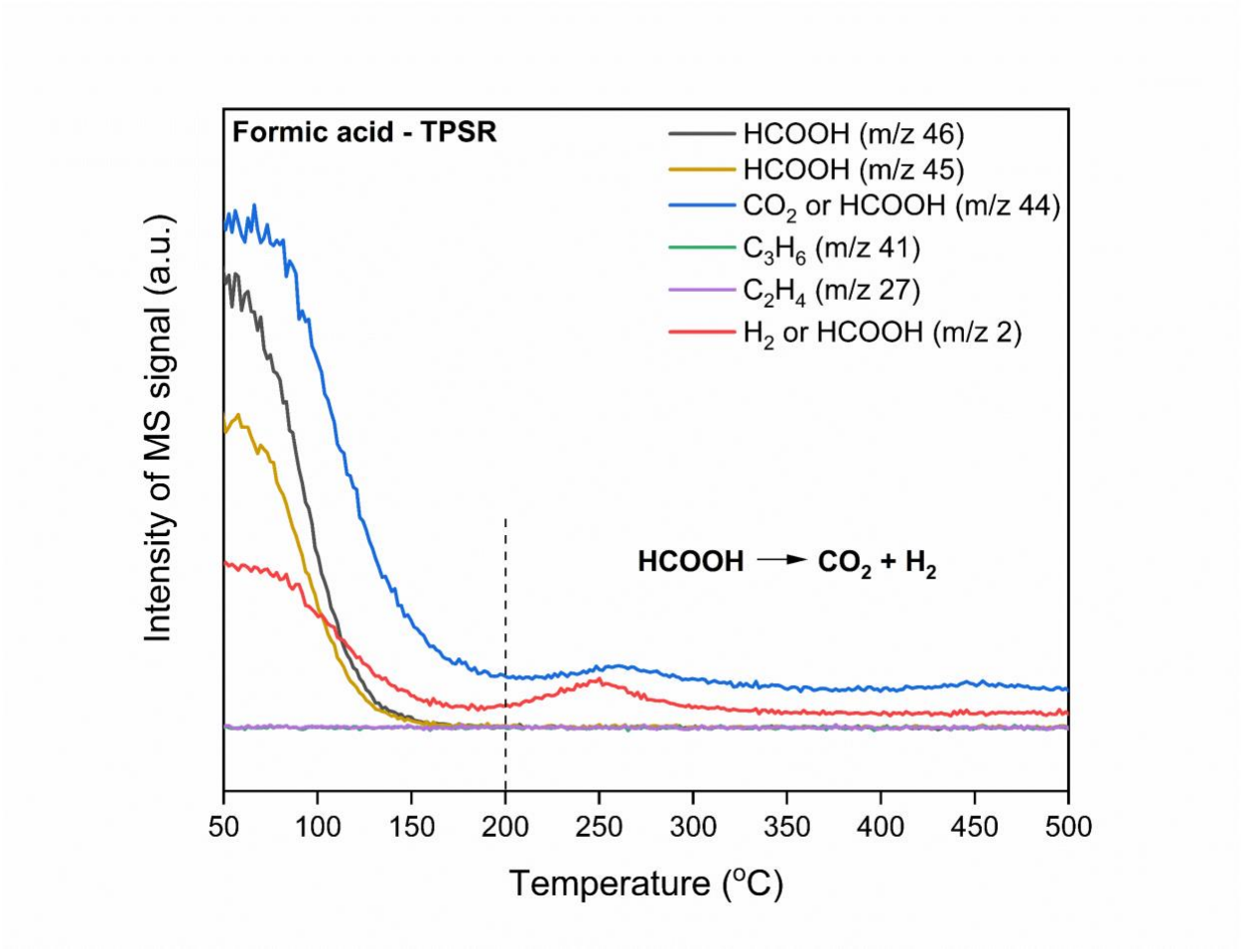

Fig. S6. Desorbed products in gas phase for the formic acid–TPSR process. Decomposition of formic acid leads to carbon dioxide and hydrogen, starting from 200 °C, whereas olefins were not observed during the whole process. Note that HCOOH can produce fragment signals at *m*/*z* 2 and 44 as well, which may overlap with the real signals of H_2 and CO_2. However, at 200 °C, the two signals at *m*/*z* 46 and *m*/*z* 45 (which also represent HCOOH) disappeared, indicating the absence of HCOOH in the gas phase. Meanwhile, we observed the simultaneous increase of *m*/*z* 2 and *m*/*z* 44 signals, indicating the occurrence of formic acid decomposition.

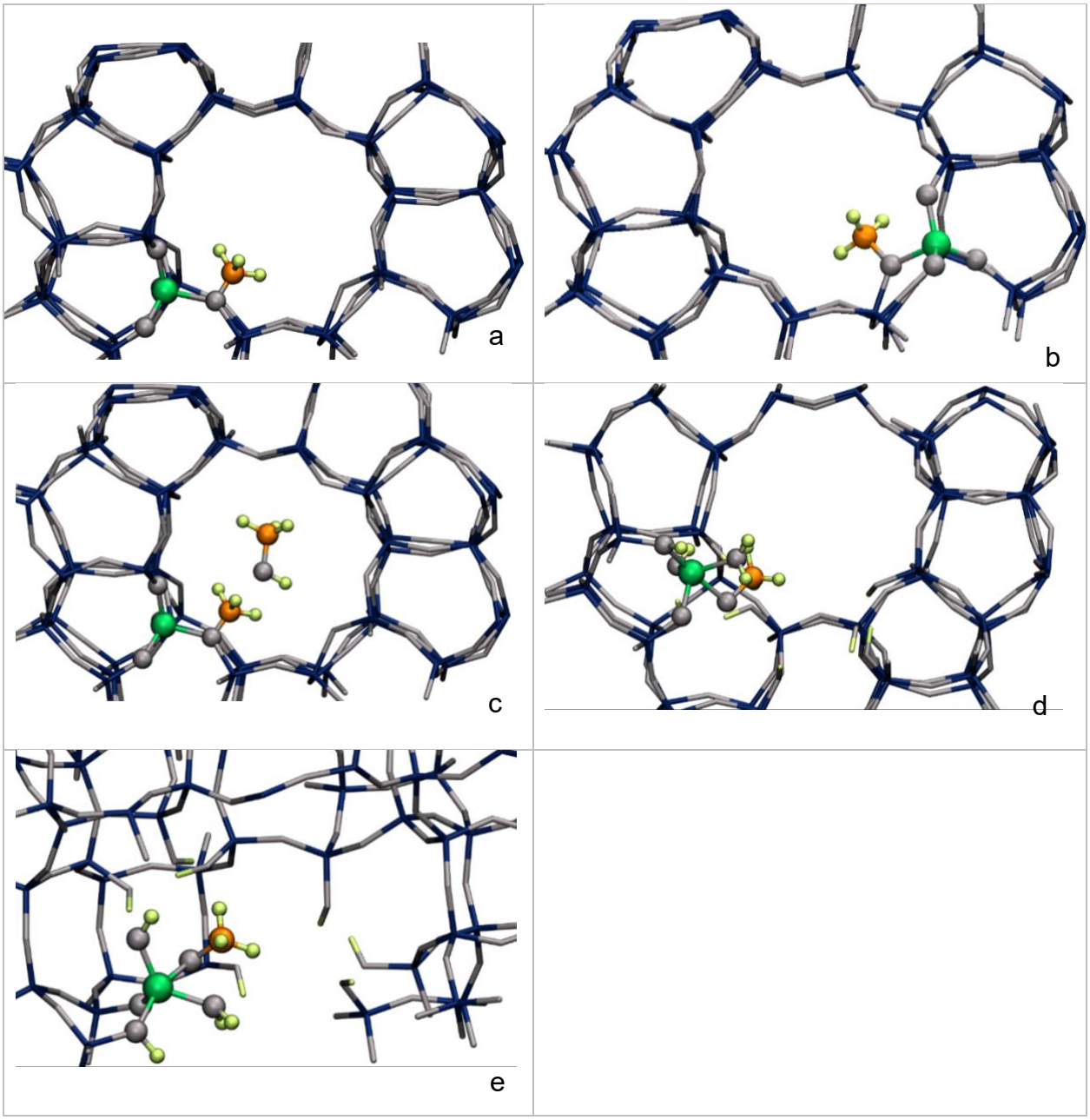

Fig. S7. Models used to determine zeolite bound methoxy vibrational frequencies. (a) Brønsted acid site methoxy, (b) T8 Brønsted acid site methoxy, (c) Brønsted acid site methoxy and methanol, (d) defect bound methoxy side view, and (e) defect bound methoxy top view. Al – green, Si – blue, O – grey, C – orange, H – yellow.

Supplementary Note 1| *Vibrational analysis discussion.* The differences between the experimentally obtained vibrational frequencies attributed to two kinds of methoxy groups detected at 2980, 2868 cm^{-1} and 2971, 2863 cm^{-1} were analyzed using the theoretical method

discussed in SI. The initial assumption was that the two sets of frequencies appear because of the heterogeneity in types of T-sites part of the H-ZSM-5 structure, therefore methoxy groups on two different T-sites were analyzed (Fig. S7a, b). In addition, previous studies highlighted that the 2971, 2863 cm^{-1} frequencies disappear when using a feed with a lower methanol per acid site ratio[23] which indicated the possibility that the interaction of methoxy with the excess methanol might exert some differences, so a model having methanol adsorbed on methoxy was also simulated (Fig. S7c). Finally, previous experimental and theoretical analyses found that the most feasible zeolite defect to exist and catalyze methanol dehydration is an intra-framework aluminum having two OH dangling bonds[24] so the model presented in Fig. S7d, e was also included in our analysis. The results summarized in Table S1 indicate that even though there is a difference in the asymmetric vibrational frequencies of the methoxy groups bonded on T12 and T8 sites, the CH_3 symmetric vibrational frequency remains the same. Opposing results stem from the methoxy groups interacting with methanol or on intra-framework zeolite defect, with the CH_3 symmetric vibrational frequencies being significantly blue or red shifted. The lack of confirmation coming from the range of models with methoxy bonded on typical zeolite active sites indicates that the 2971, 2863 cm^{-1} could come from a methoxy bonded on a zeolite defect, the identity of which remains unclear.

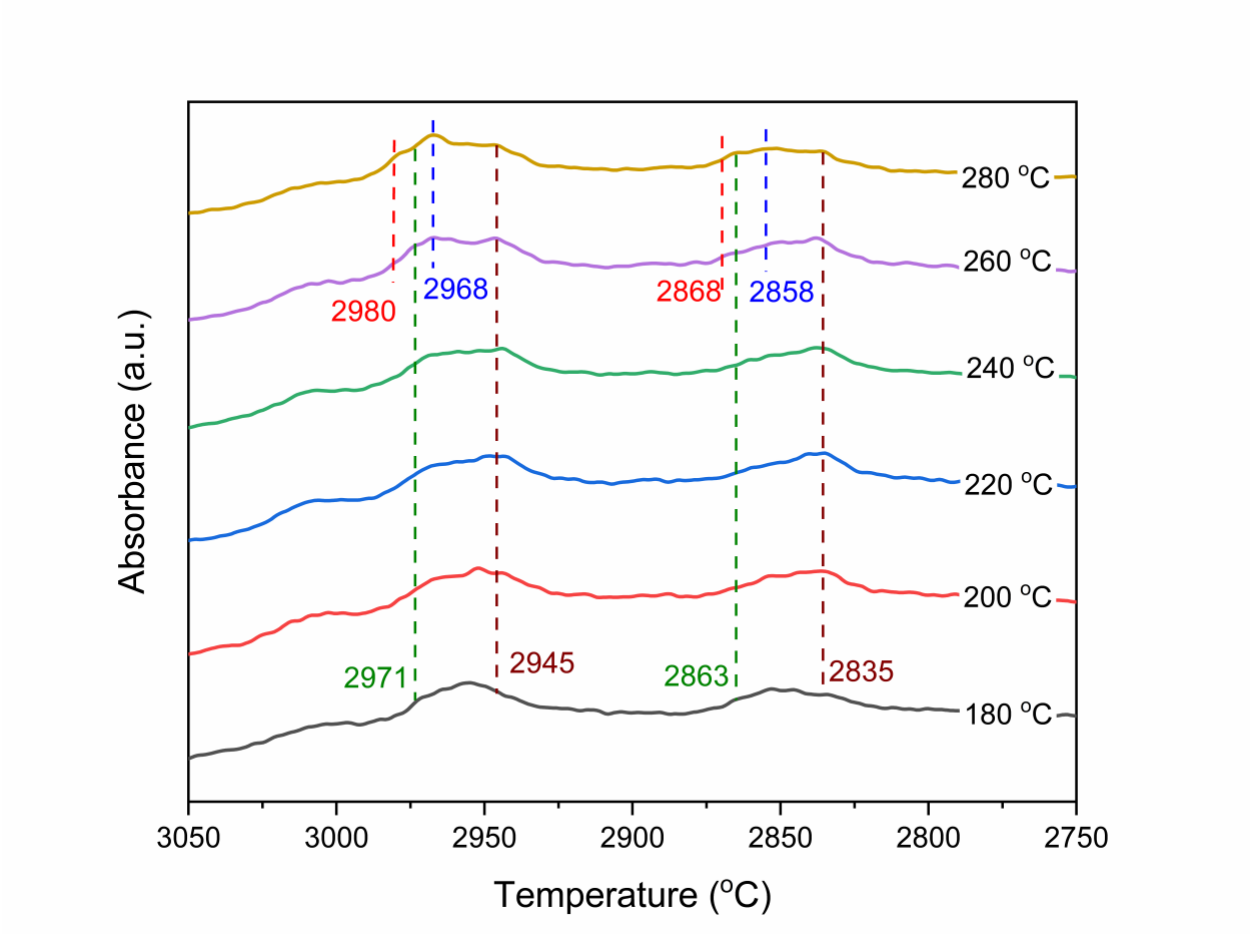

Fig. S8. *Operando* DRIFTS spectra taken during methanol–TPSR between 180 and 280 °C.

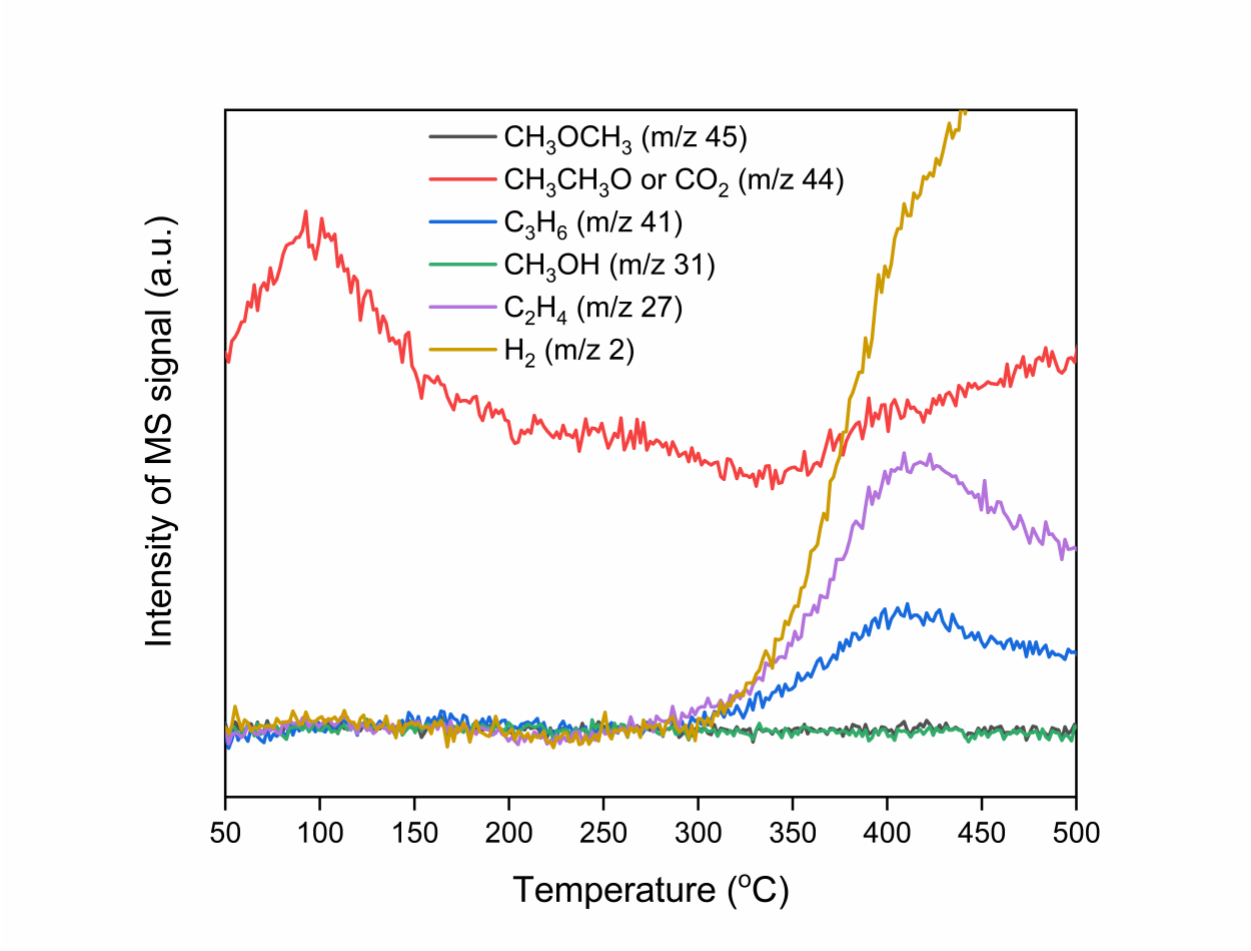

Fig. S9. Desorbed products in gas phase for the acetaldehyde–TPSR process. We observed an increase of *m*/*z* 41above 300 °C, indicative of propylene formation. Neither methanol (*m*/*z* 31) nor DME (*m*/*z* 45) signal was observed. Reaction pathways from acetaldehyde to olefins have been proposed by Li and coworkers[18, 25].

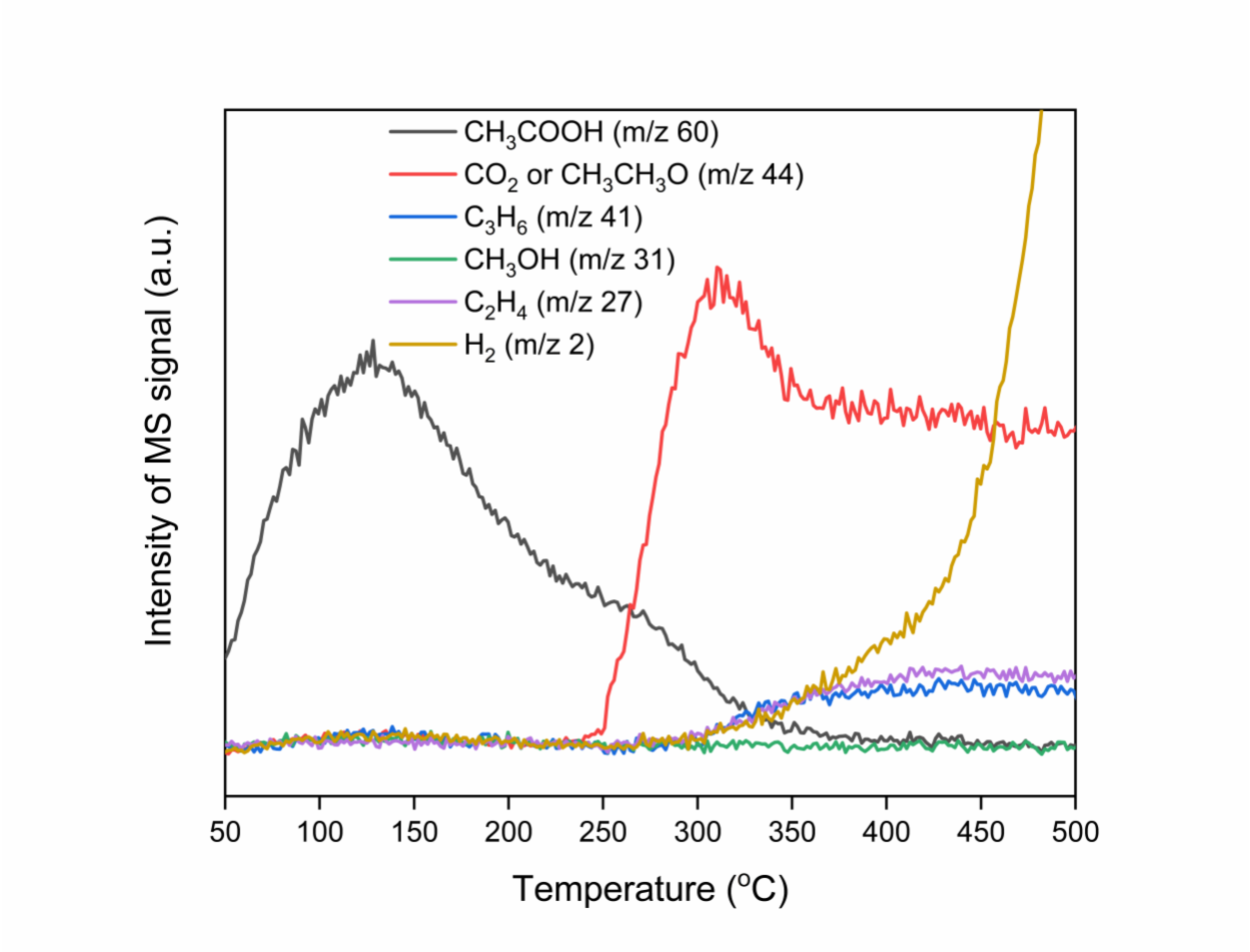

Fig. S10. Desorbed products in gas phase for the acetic acid–TPSR process. Above 250 °C, we observed an increase of the *m*/*z* 44 signal, originating from CO_2 produced via acetic acid disproportionation. Like in the case of acetaldehyde, olefin signals started to appear above 300 °C, while methanol was not observed.

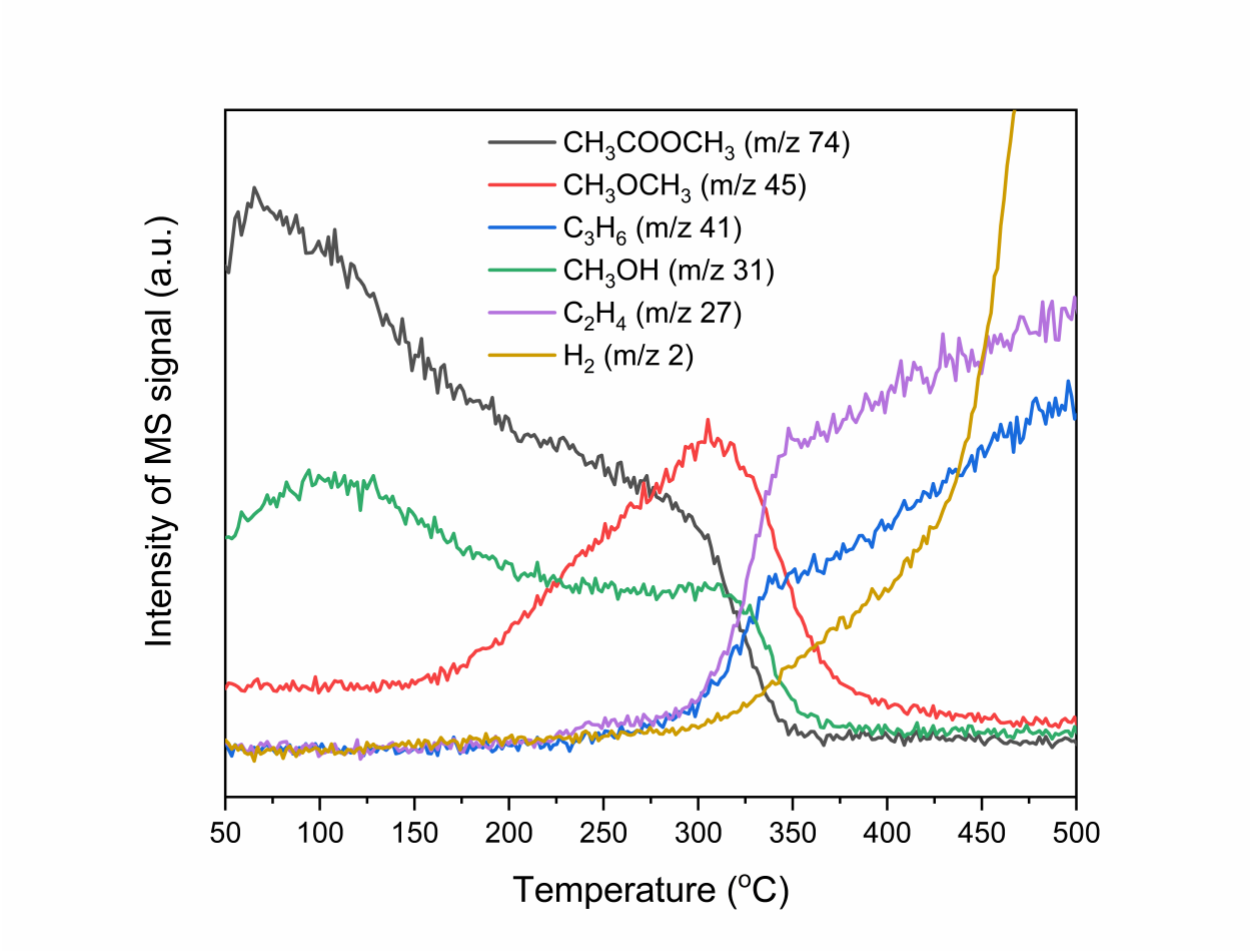

Fig. S11. Desorbed products in gas phase for the methyl acetate–TPSR process. Above 230 °C, we observed the *m*/*z* 27 and *m*/*z* 41 signals simultaneously, although they increased slowly with temperature at first. Methanol (*m*/*z* 31) and DME (*m*/*z* 45) were observed during heating and their existence appeared to promote the olefins formation at a lower temperature.

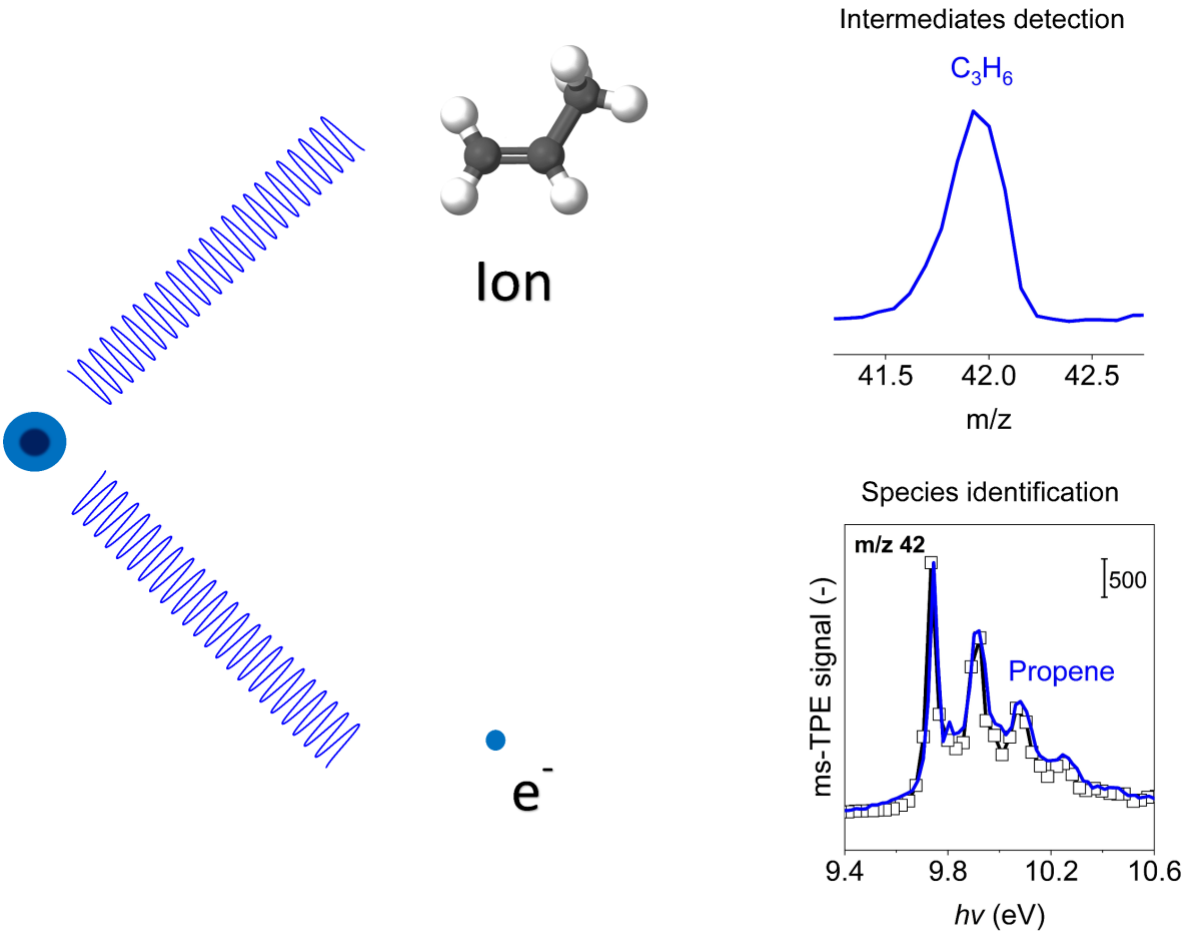

Fig. S12. Principle of *operando* PEPICO to detect and identify species. Mass spectrometry with tunable vacuum ultraviolet (VUV) synchrotron radiation establishes *m*/*z* peaks of neutrals, and photoion mass-selected threshold photoelectron (ms-TPE) spectroscopy reveals spectroscopic fingerprints for each of the *m*/*z* channels to assign the species unequivocally and isomer-specifically.

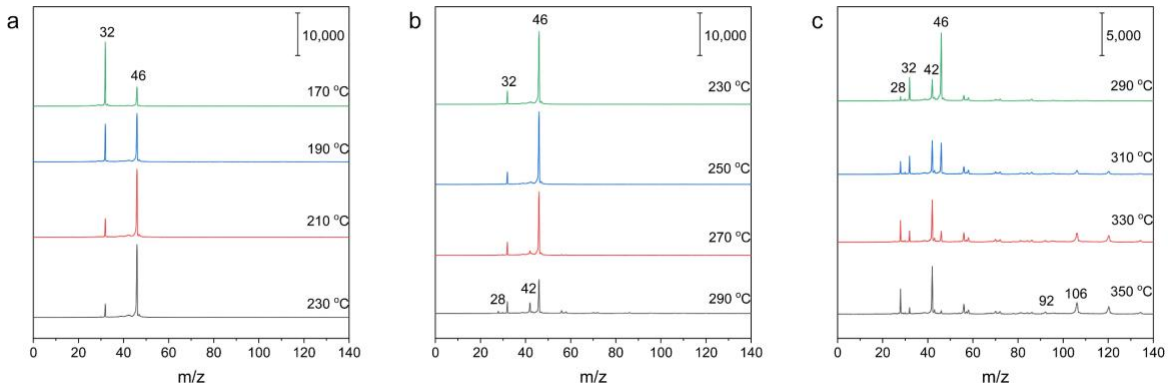

Fig. S13. Collection of photoionization mass spectra taken for methanol–TPSR with a continuous methanol flow over HZSM-5, employing a photon energy of 11 eV. Temperature range, 170–350 °C; ramp, 5 °C min^{-1}.

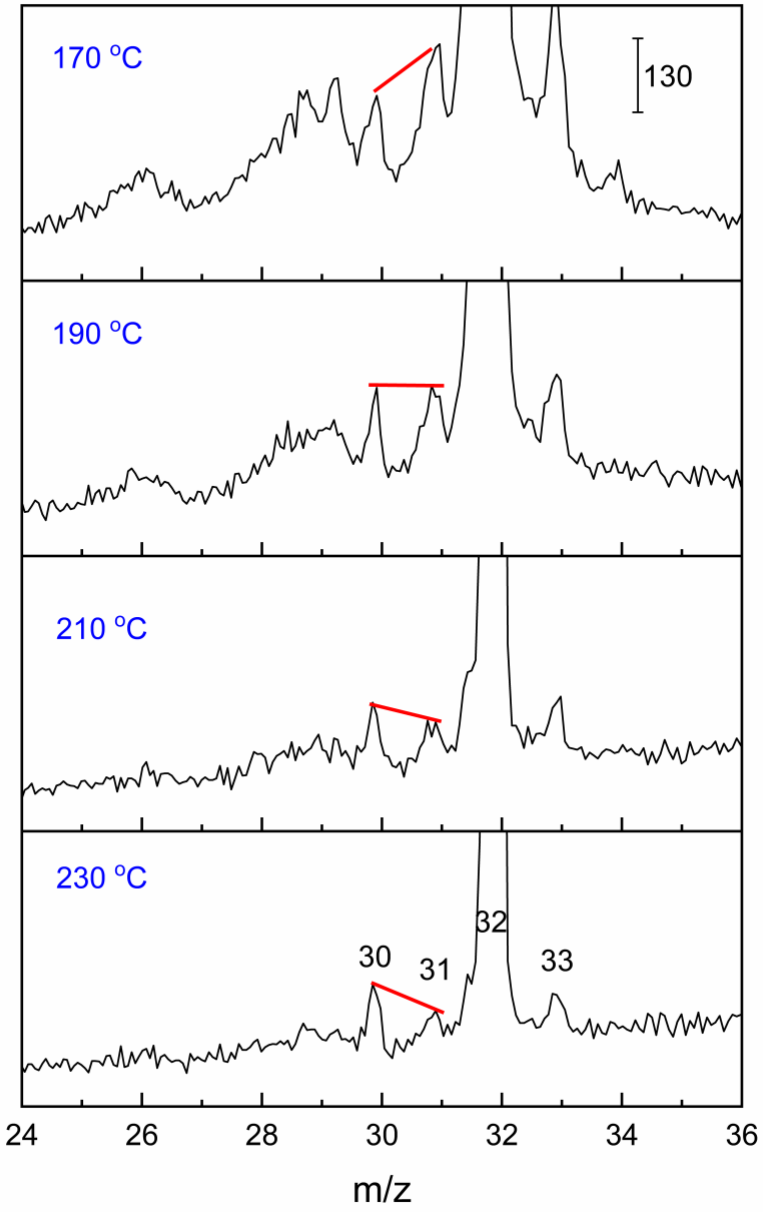

Fig. S14. Photoionization mass spectra taken for methanol–TPSR with a continuous methanol flow over HZSM-5, employing a photon energy of 11 eV. Temperature range, 170–230 °C; ramp, 5 °C min^{-1}. Between 170 and 230 °C, olefins were not observed. The photon energy of 11 eV is slightly larger than the ionization energy (IE) of methanol (10.84 eV) and that of formaldehyde (10.88 eV). As *m*/*z* 32 (CH_3OH^+) signal decreased, *m*/*z* 33 ($^{13}CH_3OH^+$) and *m*/*z* 31 (CH_3O^+, fragment) signals decreased proportionally. In contrast, *m*/*z* 30 signal did not follow this trend, indicating that *m*/*z* 30 had a different contributor, formaldehyde ($HCHO^+$). As the temperature increased, we can see more formaldehyde molecules were

produced. The PEPICO results confirm that formaldehyde can be produced at lower temperatures while olefins have not been generated yet.

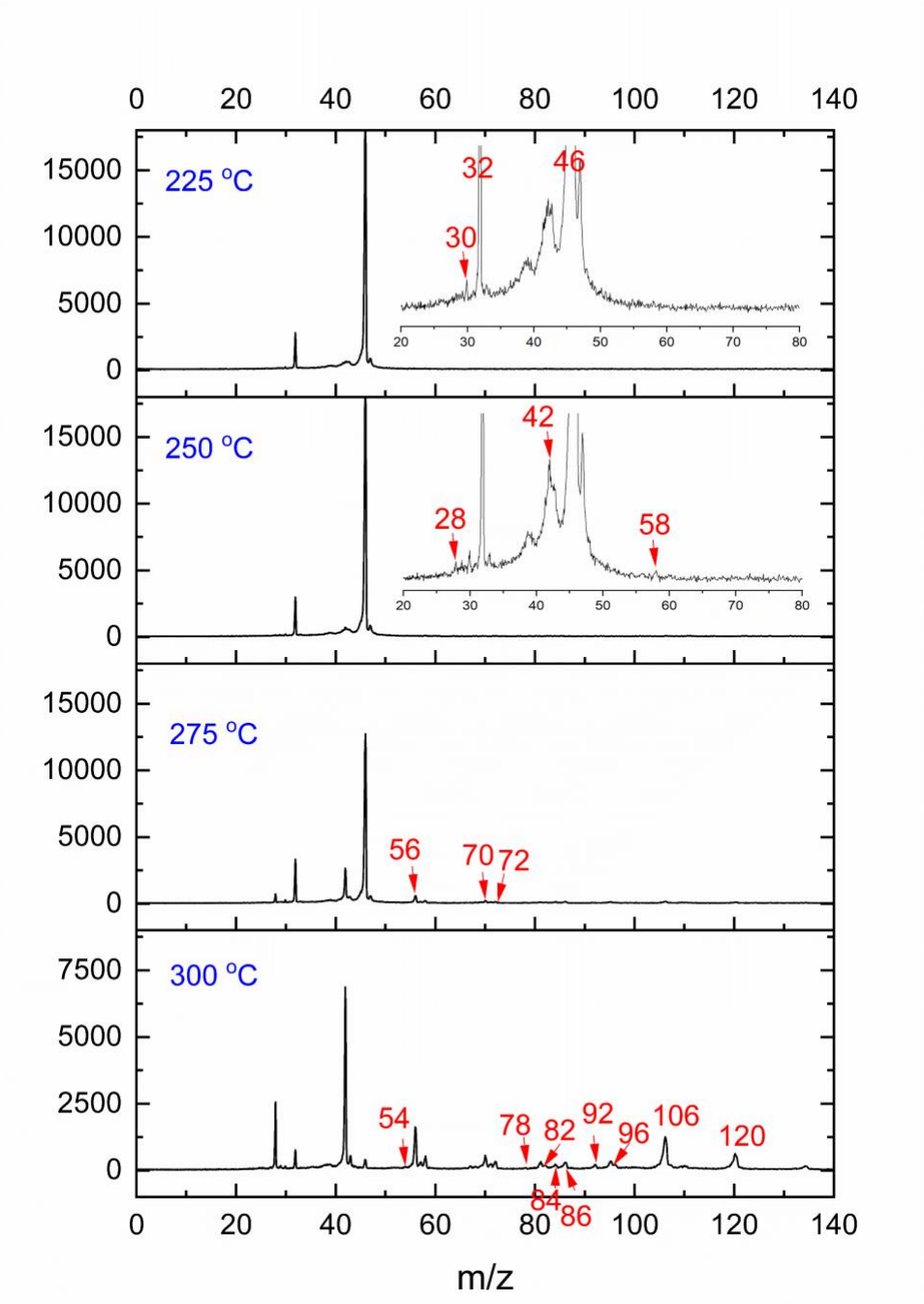

Fig. S15. Photoionization mass spectra taken for isothermal reactions, recorded at a photon energy of 11 eV.

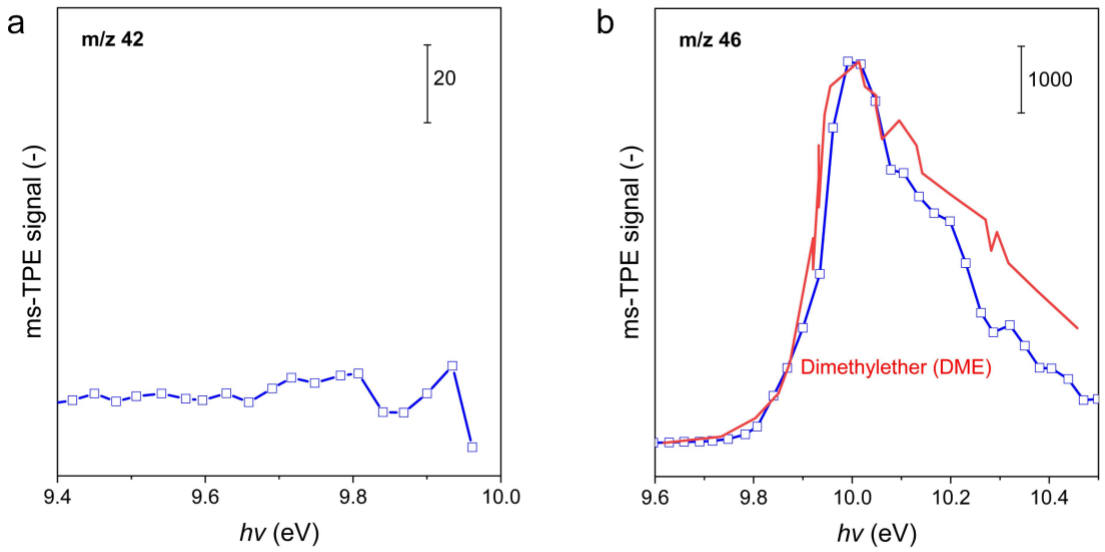

Fig. S16. ms-TPE spectra collected at 225 °C. (a) *m*/*z* 42, and (b) *m*/*z* 58 . DME (*m*/*z* 46, IE ~10.03 eV) can be detected while propene (*m*/*z* 42, IE ~9.75 eV) was absent.

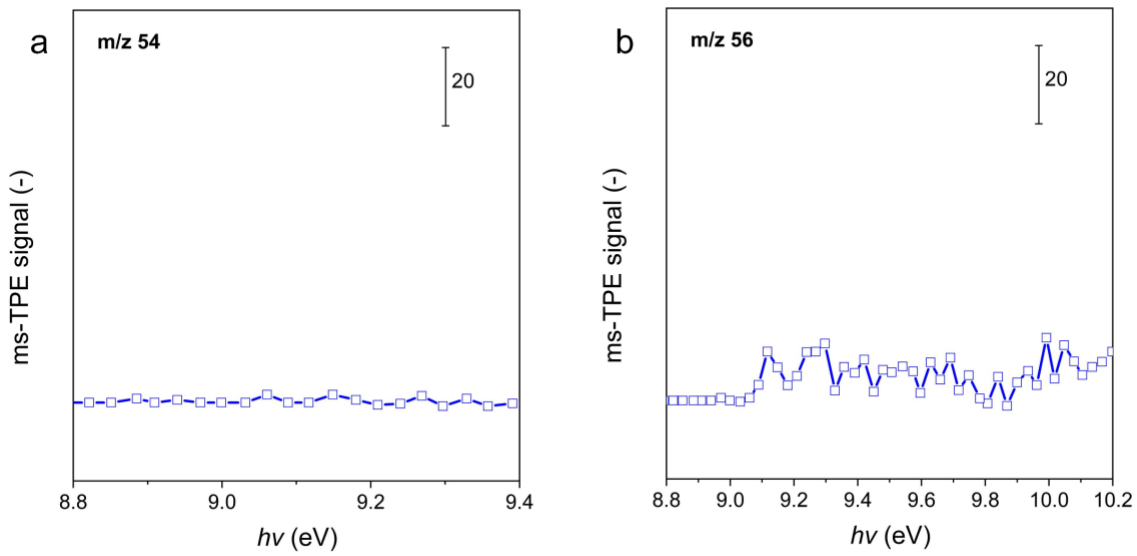

Fig. S17. ms-TPE spectra collected at 250 °C. (a) *m*/*z* 54, and (b) *m*/*z* 56. The absence of distinguishable peaks indicates that neither butadiene (*m*/*z* 54, IE ~9.07 eV) nor butenes (*m*/*z* 56) was generated above the detection limit.

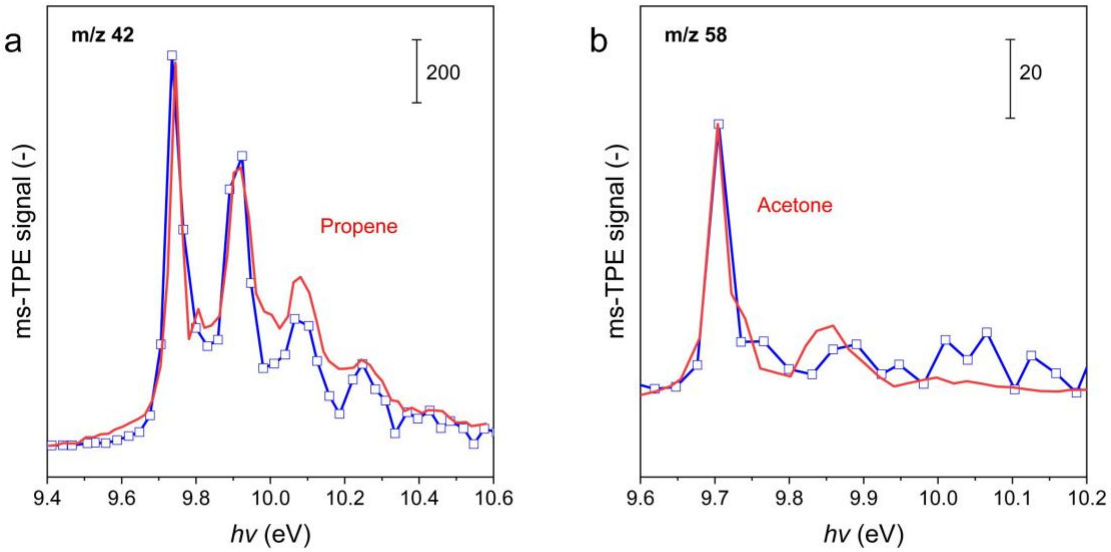

Fig. S18. ms-TPE spectra collected at 275 °C. (a) *m*/*z* 42, and (b) *m*/*z* 58. For *m*/*z* 42, the spectrum matches the simulated propene spectrum (in red) exactly. Therefore, only propene (IE ~9.75 eV) was observed while ketene (IE ~9.60 eV) cannot be observed any longer. For m/z 58, acetone (CH_3COCH_3, IE ~9.70 eV) was the dominant contributor, and the experimental spectrum matches the simulated acetone spectrum (in red), while propanal (CH_3CH_2CHO, IE ~9.96 eV) was absent.

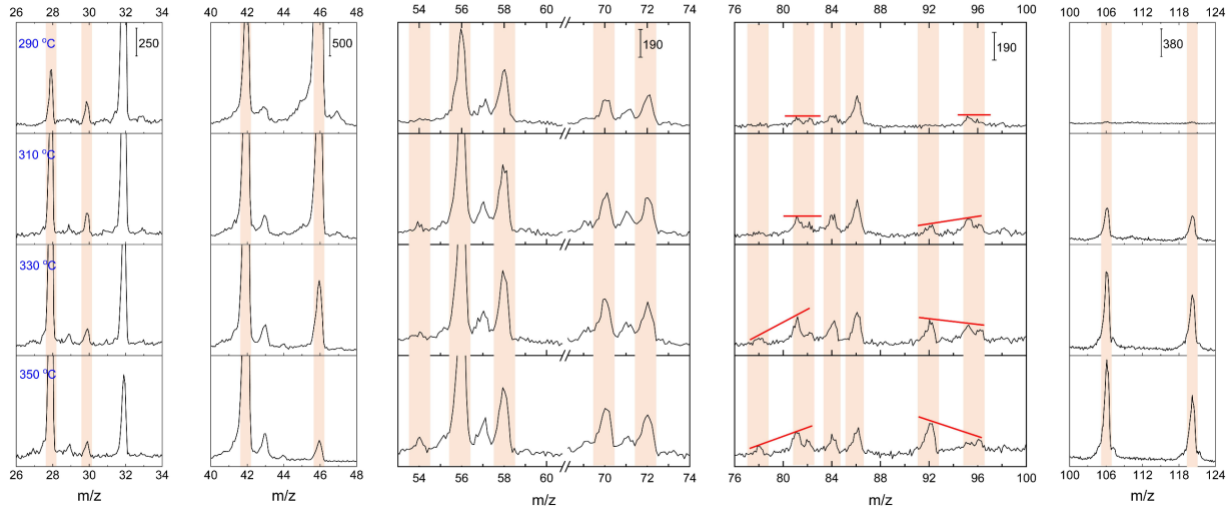

Fig. S19. Photoionization mass spectra taken for methanol–TPSR with a continuous methanol flow over HZSM-5, employing a photon energy of 11 eV. Temperature range, 290–350 °C; ramp, 5 °C min^{-1}. The red lines indicate the transformation trend from m/z 96 to m/z 92, and from m/z 82 to m/z 78.

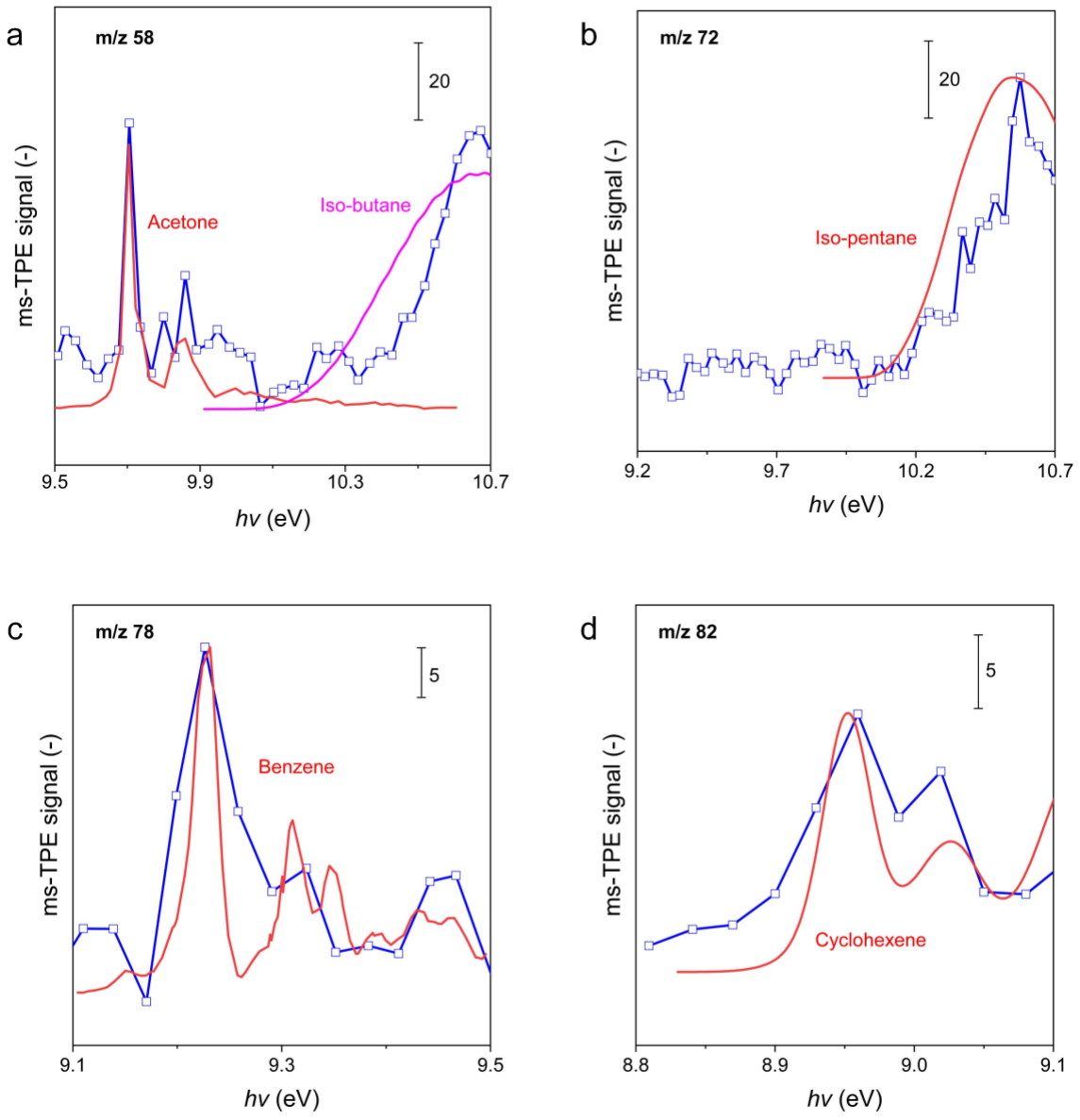

Fig. S20. ms-TPE spectra collected at 300 °C. (a) *m*/*z* 58, (b) *m*/*z* 72, (c) *m*/*z* 78, and (d) *m*/*z* 82. Simulated spectra of representative components are show in non-blue colors. For *m*/*z* 58, besides acetone (CH_3COCH_3, IE ~9.70 eV), iso-butane (C_4H_{10}, IE ~10.68 eV) was also detected. For *m*/*z* 72, butanone ($CH_3COCH_2CH_3$, IE ~9.55 eV) was not detected, while iso-pentane (C_5H_{12}, IE ~10.68 eV) became dominant. The detection of alkanes implies hydrogen transfer reactions, in parallel with aromatics production. The *m*/*z* 78 peak can be attributed to benzene (C_6H_6, IE ~9.24 eV), and the *m*/*z* 82 peak to cyclohexene (C_6H_{10}, IE ~8.95 eV).

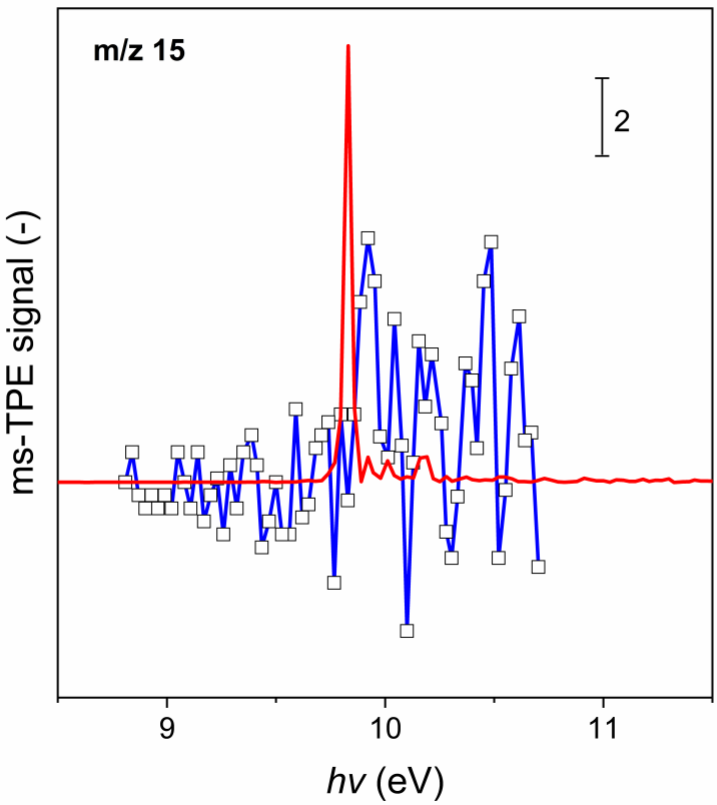

Fig. S21. ms-TPE spectra for m/z 15. Methyl radicals are not observed since the experimental spectrum (in blue) is noisy and different from the simulated spectrum (in red).

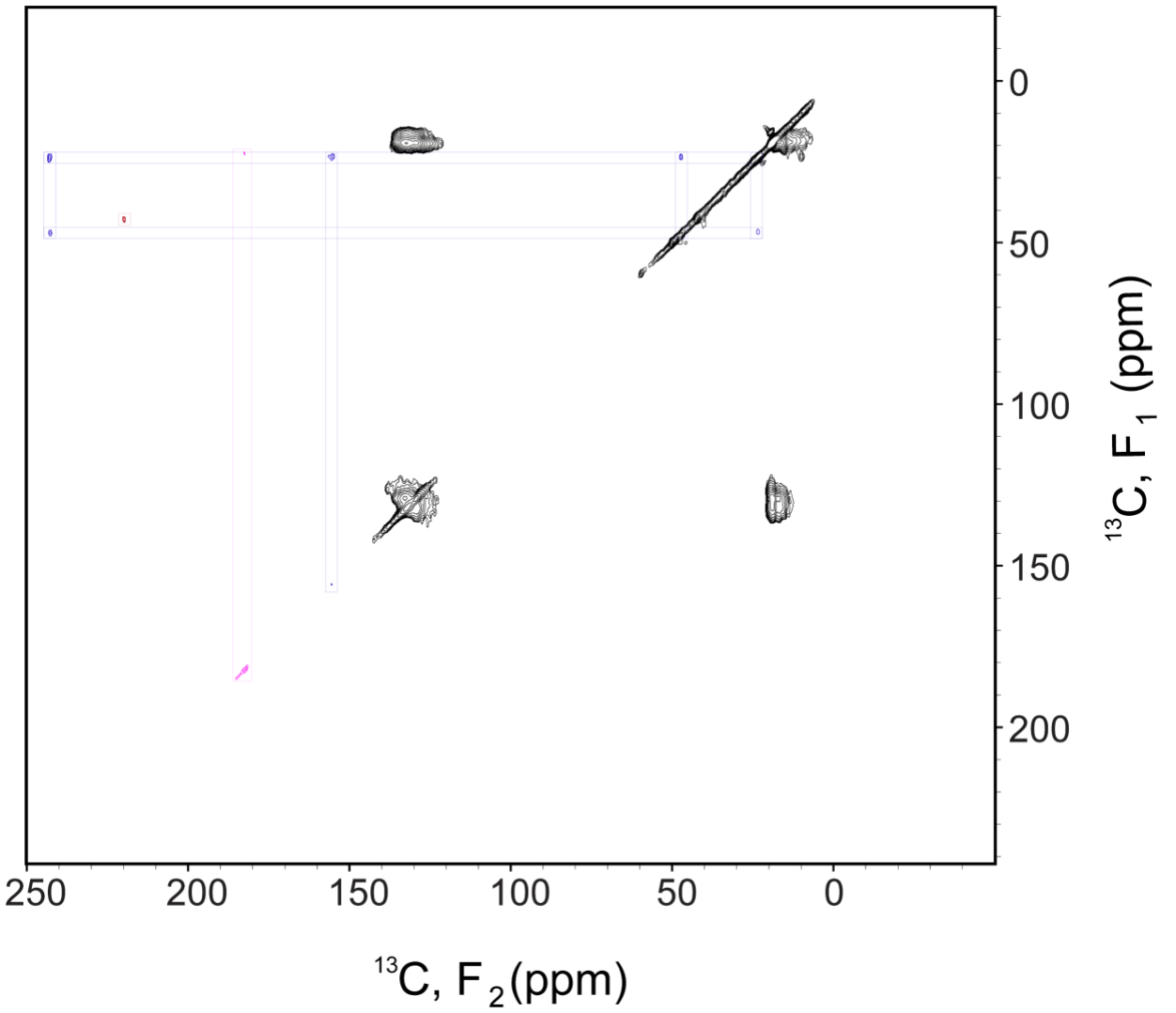

Fig. S22. 2D ^{13}C-^{13}C correlation MAS ssNMR spectrum over the sample obtained after reaction at 300 °C.

Supplementary Note 2│ Thanks to the efforts devoted to identifying the nature and the role of species produced in the MTH process, the reaction mechanism for the steady-state reaction period has been gradually revealed. Dahl and Kolboe first proposed a "hydrocarbon pool" mechanism[26], and claimed that hydrocarbon pool species could produce light olefins, alkanes, and aromatics. The dual cycle concept originated from hydrocarbon pool theory. The dual-cycle concept can explain a multitude of experimental results obtained with various zeolites topologies[27]. The olefin products can be generated by methylation and cracking of alkenes (alkenes-based cycle), or by methylation and dealkylation of aromatics (aromatics-based cycle). The alkenes- and aromatics-based cycles are interdependent, and they "communicate" through olefin cyclization and aromatic dealkylation steps[28]. In the aromatic cycle, two routes have been proposed for olefin generation from methylbenzenes, namely the side-chain[29, 30, 31] and the paring routes[29, 32, 33]. The side-chain route proceeds with methylation and the elimination of side-chain groups from the benzene rings. The paring route mechanism involves the contraction of six-membered ring cations (polymethylbenzenium cations) to five-membered ring cations (polymethylcyclopentenyl cations). Recently, more and more

evidence suggests that, instead of acting as paring route intermediates, the five-membered ring cations can produce olefins via an alternate way[34, 35, 36, 37]. Specifically, the side-chains of cyclopentenyl cations are able to be methylated into ethyl-, propyl-, and butyl-substituted cyclopentenyl cations, and the olefins can be split off subsequently. As a result, another cycle, namely the methylcyclopentenyl (MCP)-based cycle, was proposed and considered as a bridge between the alkenes- and aromatics-based cycles[35]. The formation of hydrocarbon pool species via oxygen-containing unsaturated intermediates such as acetaldehyde and acetone has also been proposed[18, 25, 38]. The aldol condensation of these intermediates could lead to heavy chain or cyclic unsaturated aldehydes/ketones. These species can be subsequently converted to alkenes via decarbonylation or to aromatics via cyclization and hydrogen transfer steps.

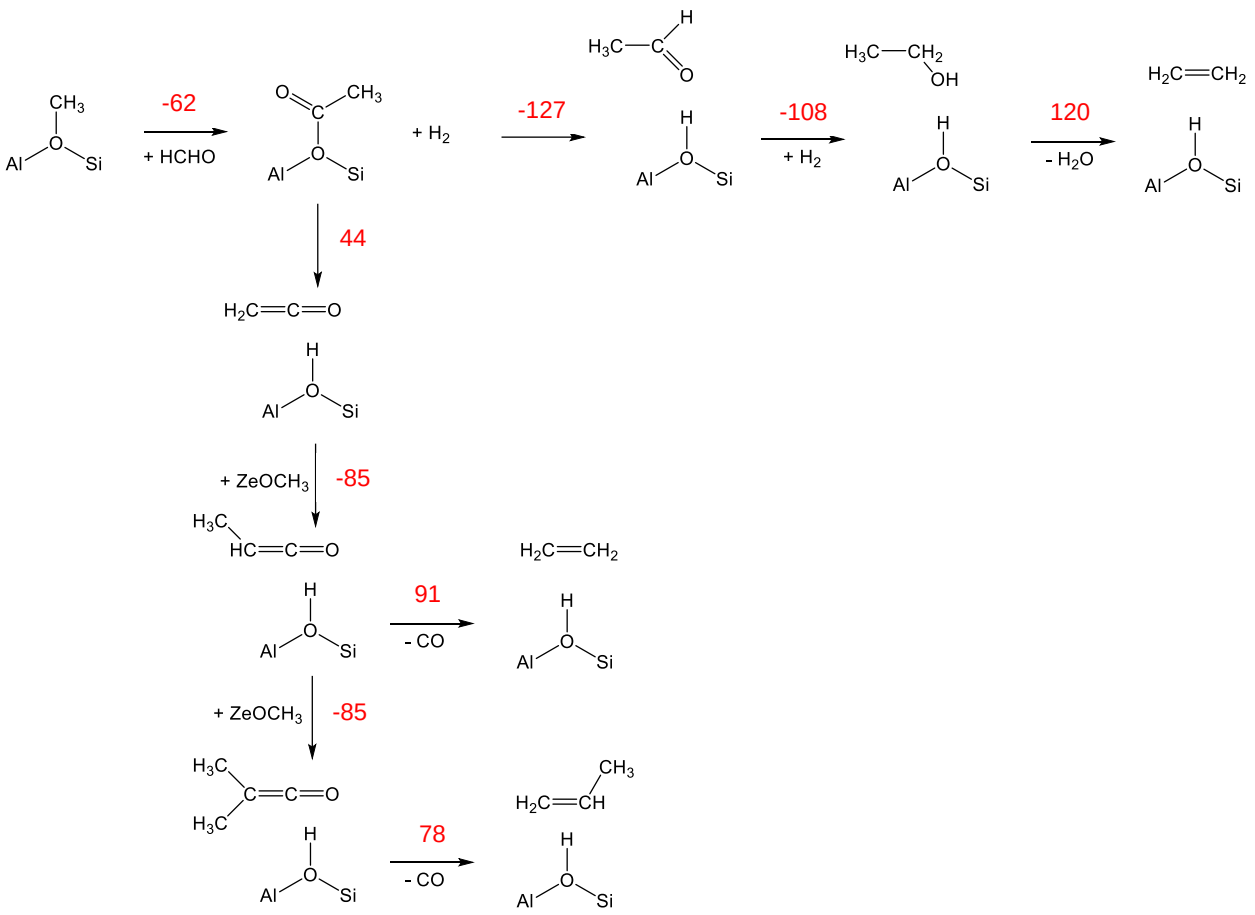

Fig. S23. Reaction routes to ethene and propene formation via acetaldehyde or ketene, with reaction energies presented in kJ/mol.

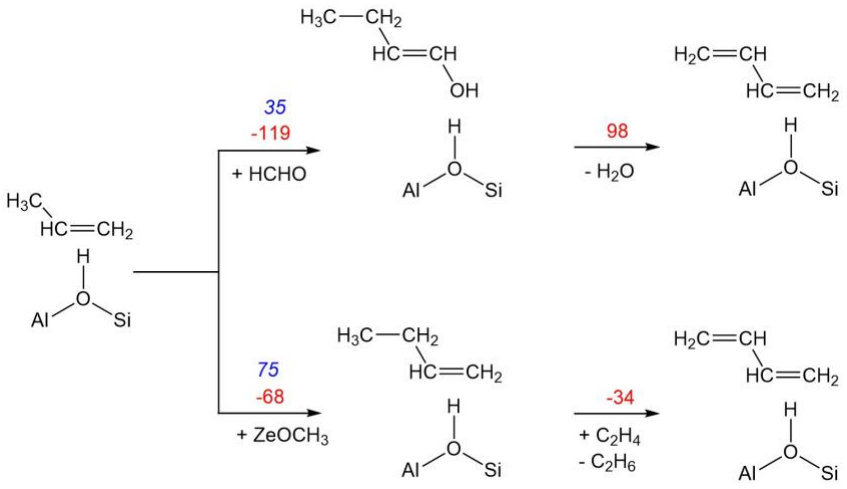

Fig. S24. Reaction routes to butadiene via propene Prins reaction followed by dehydration or propene methylation followed by hydrogen transfer, with calculated reaction energies (red) and referenced activation barriers (blue, italic)[39, 40] presented in kJ/mol.

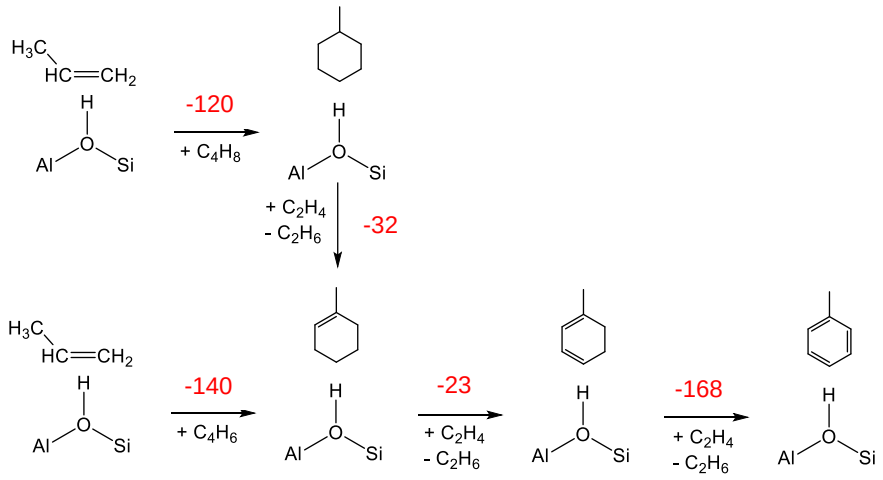

Fig. S25. Reaction routes to toluene via propene-butene oligomerization or propene-butadiene Diels–Alder reaction, with reaction energies presented in kJ/mol.

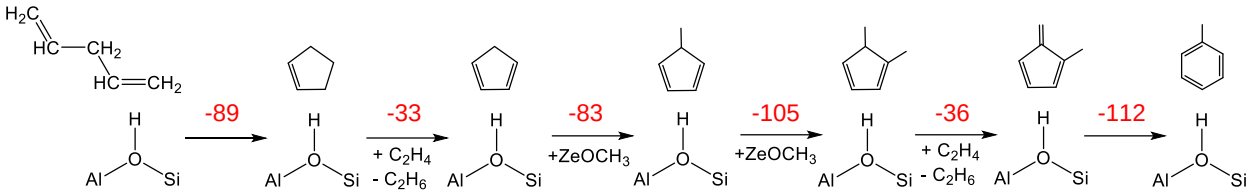

Fig. S26. Reaction route to toluene via pentadiene and cyclopentadiene, with reaction energies presented in kJ/mol.

SIII │Supplementary Table

Table S1. Summary of CH_3 symmetric (ν_s) and asymmetric (ν_{as}) vibrational frequencies in cm^{-1}.

	methoxy	methoxy (T8)	methoxy/methanol	methoxy/methanol*	methoxy defect
ν_{as}	2964	2977	2991	2903	2924
ν_{as}	2960	2955	2975	2854	2825
ν_s	2868	2869	2885	2801	2744

*Methanol vibrational frequencies

SIV │Supplementary References

1. Lee, W., Rahimi, M., Lee, Y. & Chiu, A. POKY: a software suite for multidimensional NMR and 3D structure calculation of biomolecules. *Bioinformatics* **37**, 3041-3042 (2021).
2. Kresse, G. & Furthmüller, J. Efficiency of ab-initio total energy calculations for metals and semiconductors using a plane-wave basis set. *Computational materials science* **6**, 15-50 (1996).
3. Kresse, G. & Hafner, J. Ab initio molecular-dynamics simulation of the liquid-metal–amorphous-semiconductor transition in germanium. *Physical Review B* **49**, 14251 (1994).
4. Perdew, J.P., Burke, K. & Ernzerhof, M. Generalized gradient approximation made simple. *Physical review letters* **77**, 3865 (1996).
5. Grimme, S., Antony, J., Ehrlich, S. & Krieg, H. A consistent and accurate ab initio parametrization of density functional dispersion correction (DFT-D) for the 94 elements H-Pu. *The Journal of chemical physics* **132**, 154104 (2010).
6. Kresse, G. & Joubert, D. From ultrasoft pseudopotentials to the projector augmented-wave method. *Physical review b* **59**, 1758 (1999).
7. John, M., Alexopoulos, K., Reyniers, M.-F. & Marin, G.B. Effect of zeolite confinement on the conversion of 1-butanol to butene isomers: mechanistic insights from DFT based microkinetic modelling. *Catalysis Science & Technology* **7**, 2978-2997 (2017).
8. Ghorbanpour, A., Rimer, J.D. & Grabow, L.C. Periodic, vdW-corrected density functional theory investigation of the effect of Al siting in H-ZSM-5 on chemisorption properties and site-specific acidity. *Catalysis Communications* **52**, 98-102 (2014).
9. Ramirez, A. *et al.* Selectivity descriptors for the direct hydrogenation of CO2 to hydrocarbons during zeolite-mediated bifunctional catalysis. *Nature Communications* **12**, 5914 (2021).
10. Li, T. *et al.* Influence of active-site proximity in zeolites on Brønsted acid-catalyzed reactions at the microscopic and mesoscopic levels. *Chem Catalysis* (2023).

11. Nastase, S., O'Malley, A., Catlow, C.R.A. & Logsdail, A.J. Computational QM/MM investigation of the adsorption of MTH active species in HY and H-ZSM-5. *Physical Chemistry Chemical Physics* **21**, 2639-2650 (2019).

12. Nastase, S.A., Catlow, C.R.A. & Logsdail, A.J. QM/MM study of the stability of dimethyl ether in zeolites H-ZSM-5 and HY. *Physical Chemistry Chemical Physics* **23**, 2088-2096 (2021).

13. Haase, F. & Sauer, J. Interaction of methanol with Broensted acid sites of zeolite catalysts: an ab initio study. *Journal of the American Chemical Society* **117**, 3780-3789 (1995).

14. Kotrla, J. *et al.* Hydrogen bonding of methanol with bridged OH groups of zeolites: ab initio calculation, 1H NMR and FTIR studies. *The Journal of Physical Chemistry B* **102**, 2454-2463 (1998).

15. Goodrow, A. & Bell, A.T. A theoretical investigation of the selective oxidation of methanol to formaldehyde on isolated vanadate species supported on titania. *The Journal of Physical Chemistry C* **112**, 13204-13214 (2008).

16. Hemelsoet, K. *et al.* Experimental and theoretical IR study of methanol and ethanol conversion over H-SAPO-34. *Catalysis today* **177**, 12-24 (2011).

17. Pérez-Ramírez, J. *et al.* Physicochemical characterization of isomorphously substituted FeZSM-5 during activation. *Journal of Catalysis* **207**, 113-126 (2002).

18. Yang, L. *et al.* Role of acetaldehyde in the roadmap from initial carbon–carbon bonds to hydrocarbons during methanol conversion. *ACS Catalysis* **9**, 6491-6501 (2019).

19. Paunović, V., Hemberger, P., Bodi, A., Hauert, R. & van Bokhoven, J.A. Impact of Nonzeolite-Catalyzed Formation of Formaldehyde on the Methanol-to-Hydrocarbons Conversion. *ACS Catalysis* **12**, 13426-13434 (2022).

20. Pérez-Ramírez, J. & Gallardo-Llamas, A. Impact of the preparation method and iron impurities in Fe-ZSM-5 zeolites for propylene production via oxidative dehydrogenation of propane with N2O. *Applied Catalysis A: General* **279**, 117-123 (2005).

21. Tong, Y. *et al.* HZSM-5 zeolites containing impurity iron species for the photocatalytic reduction of CO 2 with H 2 O. *Catalysis Science & Technology* **6**, 7579-7585 (2016).

22. Wen, W. *et al.* Formation and Fate of Formaldehyde in Methanol-to-Hydrocarbon Reaction: In Situ Synchrotron Radiation Photoionization Mass Spectrometry Study. *Angewandte Chemie International Edition* **59**, 4873-4878 (2020).

23. Matam, S.K., Nastase, S.A., Logsdail, A.J. & Catlow, C.R.A. Methanol loading dependent methoxylation in zeolite H-ZSM-5. *Chemical science* **11**, 6805-6814 (2020).

24. Hu, M. *et al.* Unravelling the Reactivity of Framework Lewis Acid Sites towards Methanol Activation on H-ZSM-5 Zeolite with Solid-State NMR Spectroscopy. *Angewandte Chemie* **134**, e202207400 (2022).

25. Yang, L. *et al.* Progressive steps and catalytic cycles in methanol-to-hydrocarbons reaction over acidic zeolites. *Fundamental Research* **2**, 184-192 (2022).

26. Dahl, I.M. & Kolboe, S. On the reaction mechanism for propene formation in the MTO reaction over SAPO-34. *Catalysis Letters* **20**, 329-336 (1993).

27. Olsbye, U. *et al.* Conversion of methanol to hydrocarbons: how zeolite cavity and pore size controls product selectivity. *Angewandte Chemie International Edition* **51**, 5810-5831 (2012).

28. Yarulina, I., Chowdhury, A.D., Meirer, F., Weckhuysen, B.M. & Gascon, J. Recent trends and fundamental insights in the methanol-to-hydrocarbons process. *Nature Catalysis* **1**, 398-411 (2018).

29. Xu, S. *et al.* Direct observation of cyclic carbenium ions and their role in the catalytic cycle of the methanol-to-olefin reaction over chabazite zeolites. *Angewandte Chemie International Edition* **52**, 11564-11568 (2013).

30. Sassi, A., Wildman, M.A. & Haw, J.F. Reactions of butylbenzene isomers on zeolite HBeta: Methanol-to-olefins hydrocarbon pool chemistry and secondary reactions of olefins. *The Journal of Physical Chemistry B* **106**, 8768-8773 (2002).

31. Arstad, B., Nicholas, J.B. & Haw, J.F. Theoretical study of the methylbenzene side-chain hydrocarbon pool mechanism in methanol to olefin catalysis. *Journal of the American Chemical Society* **126**, 2991-3001 (2004).

32. Bjørgen, M., Olsbye, U., Petersen, D. & Kolboe, S. The methanol-to-hydrocarbons reaction: insight into the reaction mechanism from [12C] benzene and [13C] methanol coreactions over zeolite H-beta. *Journal of Catalysis* **221**, 1-10 (2004).

33. Wang, C. *et al.* Frontispiece: New Insight into the Hydrocarbon-Pool Chemistry of the Methanol-to-Olefins Conversion over Zeolite H-ZSM-5 from GC-MS, Solid-State NMR Spectroscopy, and DFT Calculations. *Chemistry–A European Journal* **20** (2014).

34. Wulfers, M.J. & Jentoft, F.C. The role of cyclopentadienium ions in methanol-to-hydrocarbons chemistry. *Acs Catalysis* **4**, 3521-3532 (2014).

35. Zhang, W. *et al.* Methanol to olefins reaction route based on methylcyclopentadienes as critical intermediates. *ACS Catalysis* **9**, 7373-7379 (2019).

36. Hernandez, E.D. & Jentoft, F.C. Spectroscopic signatures reveal cyclopentenyl cation contributions in methanol-to-olefins catalysis. *ACS Catalysis* **10**, 5764-5782 (2020).

37. Wang, C. *et al.* Impact of temporal and spatial distribution of hydrocarbon pool on methanol conversion over H-ZSM-5. *Journal of catalysis* **354**, 138-151 (2017).

38. Ni, Y., Zhu, W. & Liu, Z. H-ZSM-5-catalyzed hydroacylation involved in the coupling of methanol and formaldehyde to aromatics. *ACS Catalysis* **9**, 11398-11403 (2019).

39. Van Speybroeck, V. *et al.* First principle kinetic studies of zeolite-catalyzed methylation reactions. *Journal of the American Chemical Society* **133**, 888-899 (2011).

40. Vasiliadou, E.S., Li, S., Caratzoulas, S. & Lobo, R.F. Formaldehyde–isobutene Prins condensation over MFI-type zeolites. *Catalysis Science & Technology* **8**, 5794-5806 (2018).